JOURNAL OF PROPULSION AND POWER
Vol. 29, No. 3, May–June 2013

Propellant Thermal Management Effect on Neutral Residence Time in Low-Voltage Hall Thrusters

Rafael A. Martinez* and Mitchell L. R. Walker†
Georgia Institute of Technology, Atlanta, Georgia 30332

DOI: 10.2514/1.B34702

The effects of anode temperature on the performance of a 4.5 kW Hall-effect thruster are investigated. The approach separates the location of gas injection from discharge current collection using an anode band, which removes the main mechanism that heats the gas distributor. A thermal model predicts a 270 K reduction of the gas distributor temperature, which corresponds to a 28% increase in the propellant residence time. Collection of the discharge current on the anode band, which is upstream of the bulk Hall current region, generates a 10% increase in ion current density at the thruster centerline for discharge voltages of 100, 125, and 150 V at a xenon mass flow rate of 5 mg/s. The initial reduction in neutral velocity with the anode band is counteracted by the influence of the channel wall temperature, which increases the neutral velocity of the particles by up to 25% greater than the velocity at the gas distributor exit plane. This reduces the potential thruster efficiency improvement from 5.5 to 2.5%. The selected downstream location of the anode band results in a 6–10% increase in discharge current compared with current collection on the gas distributor.

Nomenclature

A_C	=	Channel cross-sectional area, m^2
e	=	electron charge, C
f_i	=	fraction of ionized neutral atoms
I_b	=	beam current, A
I_d	=	discharge current, A
Kn	=	Knudsen number
k_B	=	Boltzmann's constant, $J \cdot K^{-1}$
L	=	characteristic length scale, m
L_{ch}	=	channel length, m
m	=	mass of propellant atom, kg
$\dot{m}_a$	=	anode mass flow rate, $mg \cdot s^{-1}$
$\dot{m}_b$	=	total ion mass flow rate, $mg \cdot s^{-1}$
n_e	=	electron number density, m^{-3}
n_n	=	neutral number density, m^{-3}
P_b	=	base pressure, torr
P_c	=	corrected pressure, torr
P_i	=	indicated pressure, torr
P_{input}	=	input power, kW
P_{thrust}	=	jet power, kW
T_e	=	electron temperature, K
T_n	=	neutral propellant temperature, K
V_{cg}	=	cathode to ground voltage, V
V_d	=	discharge voltage, V
V_e	=	electron velocity, $m \cdot s^{-1}$
V_i	=	ion velocity, $m \cdot s^{-1}$
V_{loss}	=	loss voltage, V
V_{mp}	=	most probable voltage, V
V_n	=	mean neutral velocity, $m \cdot s^{-1}$
V_p	=	plasma potential, V
V_{true}	=	true ion voltage, V
υ_{en}	=	electron–neutral collision frequency, s^{-1}
Z_i	=	charge state of ith ion species, 1, 2, 3, etc.
Γ	=	axial flux of neutral particles, $m^{-2} \cdot s^{-1}$
η_a	=	anode efficiency
η_b	=	current use efficiency
η_d	=	dispersion efficiency
η_p	=	propellant use efficiency
η_q	=	charge use efficiency
η_v	=	voltage use efficiency
λ	=	mean free path, m
σ_{en}	=	electron–neutral cross section, m^2
τ_i	=	characteristic ionization time, s
τ_r	=	characteristic residence time, s
Ω_i	=	current fraction of ith ion species, 1, 2, 3, etc.

I. Introduction

HALL-EFFECT thruster (HET) research and development has increased significantly in the United States over the past 20 years due to the rapid increase of in-space power, the expansion of global telecommunications, and the realization of commercial and government investment in electric propulsion technology since the early 1960s. HETs represent an effective alternative to chemical-based rocket propulsion for low-thrust propulsion applications in spacecrafts. The high thrust-to-power (T/P) ratio regime of HET operation is well suited to station keeping and orbit transfers of Earth-orbiting satellites. Military and commercial satellite programs will benefit from the large propellant mass fraction offered by this class of electric thruster [1].

Propellant use is a primary factor in determining thruster performance. Propellant use is the amount of neutral anode flow that is converted into ion flow and is expressed as [2]

$$\eta_p = \frac{\dot{m}_b}{\dot{m}_a} = \frac{mI_b}{\dot{m}_a e}\sum\frac{\Omega_i}{Z_i} \tag{1}$$

where $\dot{m}_b$ is the total ion mass flow rate, $\dot{m}_a$ is the anode mass flow rate, m is the mass of the propellant atom, I_b is the beam current, Ω_i is the current fraction of the ith ion species, and Z_i is the charge state of the ith ion species. The anode efficiency of a HET is defined by the following expression [2]:

$$\eta_a = \eta_b \eta_v \eta_p \eta_q \tag{2}$$

where η_b is the beam current fraction of discharge current, η_v is the beam voltage fraction of discharge voltage, and η_q is the charge use efficiency and is the measure of the overall charge state of the beam ions. Equation (2) shows how the efficiency of a thruster is

Received 14 June 2012; revision received 28 December 2012; accepted for publication 4 January 2013; published online 3 April 2013.

*Graduate Research Assistant, Department of Aerospace Engineering, 270 Ferst Dr. NW. Student Member AIAA.

†Associate Professor, Department of Aerospace Engineering, 270 Ferst Dr. NW. Associate Fellow AIAA.

proportional to propellant use η_p, which will increase with beam current through Eq. (1).

Wilbur and Brophy show that a cooled anode improves the propellant use of an ion thruster through an increase in the propellant residence time compared with an uncooled anode [3]. This led to the reverse injection technique used in state of the art gridded ion engines. Kieckhafer et al. used a shim anode in the HET, which allows for splitting of the discharge current between the gas distributor and an auxiliary anode [4]. They show that an increase in the shim anode current decreases the anode temperature, which causes an increase in the beam current. The authors speculate that the increase in beam current is due to increased propellant use, which may be a direct consequence of increased residence time.

Experiments have shown that an actively cooled HET anode will increase the ionization fraction through increased propellant residence time [5]. Several methods to improve propellant use have been suggested in the past, such as changes to the anode orifice size and spacing, propellant injection through the discharge channel walls, and variable discharge channel geometry [6–9]. This work aims to increase the propellant use by a reduction in the temperature of the neutral propellant as it enters the discharge chamber. Various effects that may cause the neutral particle temperature to differ from the gas distributor front face temperature inside the discharge channel are also examined. Section II presents the theory for the increase of the propellant residence time in HETs. Section III presents the thermal model used to determine the necessary changes to a HET in order to reduce the gas distributor temperature. Section IV presents the experimental setup. Section V presents the measured thruster temperature characteristics, performance, and plume properties for the conditions tested. Finally Sec. VI discusses the results and implications.

II. Theory

Power deposition to the anode is a prominent loss mechanism for HETs, and its severity will impact the anode temperature, which in turn affects neutral flow properties. To reduce the temperature of neutral propellant atoms from the gas distributor, which also serves as the anode in conventional HETs, a reduction in the thermal energy acquired by the neutral particles is needed. In continuum flow, a reduction in the propellant temperature upstream of the anode/gas distributor structure has little effect. The particles accommodate quickly to the gas distributor/anode structure temperature due to the large number of wall collisions inside the gas distributor. The work contained herein seeks to decrease the heat flux to the gas distributor from the plasma electrons through the separation of the gas distributor from the anode. This will reduce the gas distributor temperature, which will in turn decrease the neutral flow temperature. A reduction in the neutral flow temperature will reduce the axial velocity of the neutral particles and increase propellant residence time. This increase in residence time then leads to an increase in the probability of electron–neutral ionization collisions, which results in a rise in the ionization fraction.

To contribute to the thrust, a neutral propellant atom must be ionized and accelerated before it is permitted to escape the discharge chamber. The ratio of the characteristic residence time in the discharge channel (τ_r) to the characteristic ionization time (τ_i) is used to quantify the effect of neutral velocity on ion production. The characteristic residence time is taken to be proportional to channel length L_{ch} divided by the neutral velocity, $\tau_r = L_{\text{ch}}/V_n$, where V_n is the neutral atom velocity defined as the mean velocity for an assumed Maxwellian distribution given by

$$V_n = \sqrt{\frac{8k_B T_n}{\pi m}} \tag{3}$$

where T_n is the temperature of the neutral particles, k_B is Boltzmann's constant, and m is the atomic mass of the particle. Figure 1 shows the relationship of the mean neutral velocity and the characteristic resistance time with anode temperature, which is assumed to equal the temperature of the neutral particles. Without knowledge of the actual ionization zone length, the characteristic resistance time is taken to be proportional to the discharge channel length. The range of anode/gas distributor temperatures on the downstream face plotted in Fig. 1 is consistent with values measured with direct-contact thermocouples in the NASA-173Mv2 HET operating at a power of 5.5 kW, the NASA-457M HET at 50 kW, the SPT-100 HET at 1.35 kW, and the SPT-140 HET from 1.7 to 6.8 kW [6–9]. For the experiments in this paper, the thermocouples are attached to the backside of the gas distributor (the rear of the gas distributor), and a thermal model is used to determine the temperature of the downstream face.

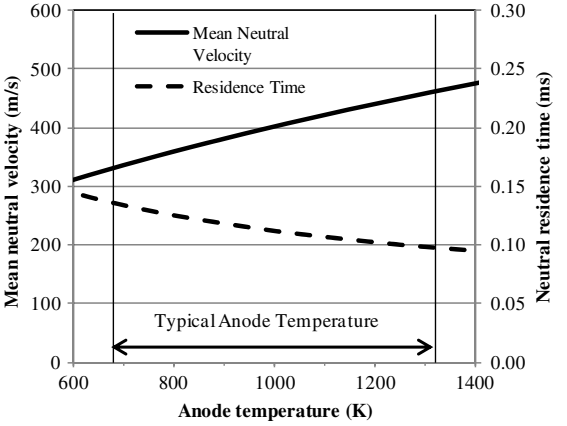

Fig. 1 Mean neutral velocity and characteristic neutral residence time as functions of anode temperature.

The mean collision time for an electron–neutral collision between electrons and neutrals is

$$\tau_i = \frac{1}{n_e \langle \sigma_{\text{en}} V_e \rangle} \tag{4}$$

where n_e is the electron number density, V_e is the electron velocity, and σ_{en} is the ionization electron–neutral cross section. The brackets represent an average over an assumed Maxwellian velocity distribution. To maximize propellant use for a given thruster design, the characteristic neutral residence time must be much larger than the ionization time ($\tau_r \gg \tau_i$). The ratio of neutral residence time to characteristic ionization time of a neutral physically represents the average number of collisions that result in ionization experienced by a propellant atom before it diffuses out of a discharge chamber of length L_{ch}. Equation (5) shows this relation:

$$\frac{\tau_r}{\tau_i} = \frac{L_{\text{ch}} n_e \langle \sigma_{\text{en}} V_e \rangle}{V_n} \tag{5}$$

For fixed channel geometry, channel material, discharge voltage, and anode mass flow rate, the only free parameter that remains in Eq. (5) is the neutral velocity. Figure 2 shows how the characteristic residence time to ionization time ratio varies as a function of anode temperature using Eq. (5). A reduction in the anode temperature, thus the propellant temperature, at a given operating condition is expected to lead to a direct increase in the propellant use. However, as the anode temperature falls below the channel base temperature, it will be the temperature of the wall immediately adjacent to the gas distributor that heats the neutrals predominantly through the mechanism of neutral–wall collisions. This effect will also be studied.

The work presented here focuses on follow-on efforts from previous work conducted by Book and Walker that uses an actively cooled anode to increase the neutral residence time [5]. Experiments with an actively cooled anode showed a 56% increase in the T/P ratio at 100 V and a reduction in the T/P ratio as voltage is increased compared with the standard anode design. At 100 V, ion current density measurements reveal an increase in ion production due to the cooled anode. However, the significant power consumption and mass of a forced convection cooling system renders a cooled-anode HET impractical for space applications. Therefore, in addition to a more

thorough diagnostic investigation into the physics that govern the relationship between anode temperature and ionization fraction, a passive mechanism is implemented in this work to achieve a significant reduction in the neutral particle velocities.

III. Thermal Modeling

A thermal model of the Pratt and Whitney Rocketdyne T-140 HET [10] was developed to study the power deposition distribution on the gas distributor and analyze the impact of the separation of the current collection site from the propellant injection site. A review of thermal models developed for HETs [11,12] and experiments on the electron current fraction of state of the art HETs [13] allows estimation of the heat flux on a HET gas distributor during normal operation. For the thermal model, it is assumed that a T-140 HET at 5 kW of discharge power will deposit 1 kW of power to the anode based on estimated inputs reported in the literature for similar HET sizes and power levels [11,12]. The design of the T-140 anode band configuration is a culmination of several models and simulations. All thermal simulations were performed in COMSOL Multiphysics version 4.3 using the heat transfer module [14]. COMSOL was used in the actively cooled anode tests with experimentally verified results [5].

To establish a thermal distribution baseline of the unmodified T-140 HET, the initial simulations evaluate the gas distributor temperature characteristics of a T-140 anode exposed to a 1 kW heat flux. The heat flux is modeled as a boundary condition on the anode face directly exposed to the plasma. Radiative and conductive heat loss to the surroundings is permitted, and the material properties are set to be consistent with the 316 stainless steel material of the anode. The thermal contact resistance or its inverse, the interfacial conductance, is estimated for each material interface in the thruster and applied to a thin artificial layer at the boundary between adjacent materials. The model results show that the downstream face of the gas distributor/anode is approximately 225 K hotter than the upstream portion of the gas distributor body, which is a result of the low thermal conductivity of stainless steel. The simulated temperature at the gas distributor exit plane is 1240 K, which is consistent with that of a similar thruster, the NASA-173M [6]. This initial thermal simulation provides a reference temperature for injected propellant for the T-140 thruster at the 5 kW power level.

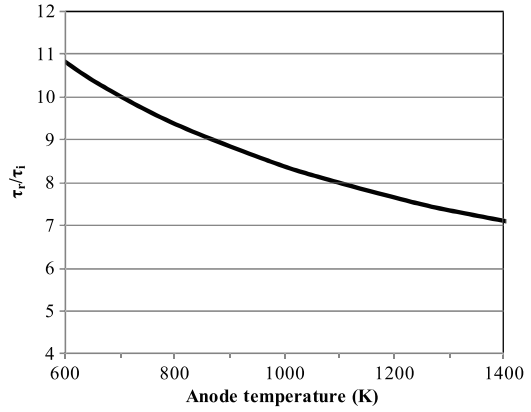

Fig. 2 Ratio of characteristic neutral residence time to characteristic ionization time as a function of anode temperature.

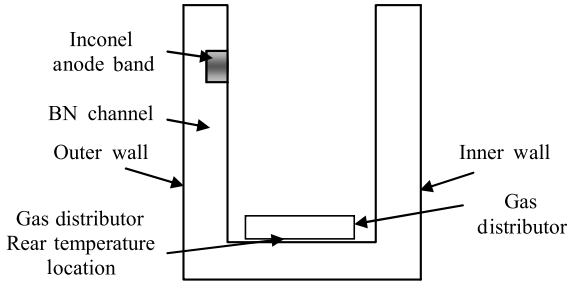

Fig. 3 Drawing of anode band location embedded in the outer wall (not to scale).

Table 1 T-140 HET thermal model inputs

Thermal model component	Thermal model inputs
Inner wall temperature downstream face	1100 K
Outer wall temperature downstream face	1040 K
All other channel surfaces	Thermally insulated
Gas distributor face heat flux	149, 250 W/m^2
Materials	
Gas distributor	SS 316L
Discharge channel	M-grade BN
Anode band	Inconel 625

Table 1 shows the thermal model inputs. Figure 4 shows the result of the thermal model when the discharge current is collected on the anode band embedded in the outer channel. COMSOL simulation results are used to estimate the average temperature at the front (exit plane) of the gas distributor for the power levels tested. The simulations predict that the effect of separating the anode from the propellant distribution site is a reduction of the gas distributor face temperature of approximately 270 K. Based on Eq. (3), the temperature reduction represents a decrease in the neutral velocity of approximately 22% and an increase in the residence time of approximately 28% compared with when the gas distributor collects the discharge current.

Figure 3 shows a sketch of the modified thruster with the inconel `anode band embedded upstream of the outer channel wall exit plane. Inconel 625 is chosen as the anode band material due to its strength over a wide temperature range. The anode band is located 12.7 mm upstream of the discharge channel exit plane. This is based on the optimum location for maximum temperature reduction and minimum interference with the Hall current region. Results from the published literature indicate that the bulk of the Hall current region is located just upstream of the peak magnetic field location and quickly decreases and flattens out axially within 15 mm of that region [15]. Although the magnetic field at the band surface is 50 G, the anode band is located in a region that corresponds to at most 15% of the peak Hall current. This location avoids interference with the bulk of the Hall current, which has been shown to have negative impact on thruster performance [16]. Furthermore, the anode band location does not affect the thruster magnetic circuit. A groove is machined into the outer BN wall, so that the inconel band sits flush with the outer wall and is large enough to account for thermal expansion.

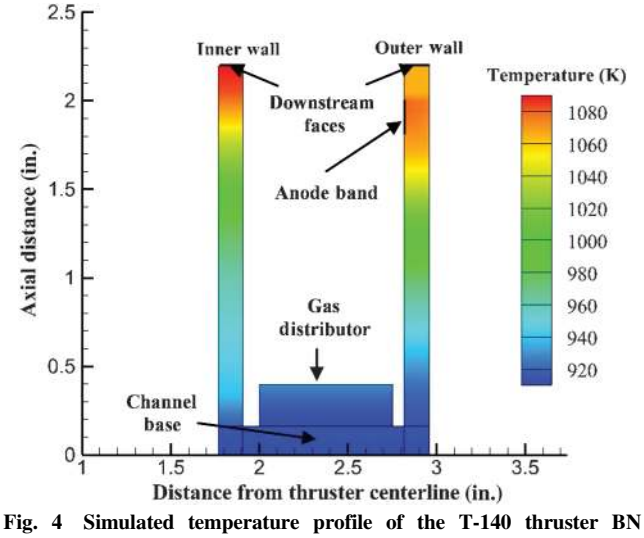

Fig. 4 Simulated temperature profile of the T-140 thruster BN discharge channel and gas distributor with the discharge current collected on the anode band.

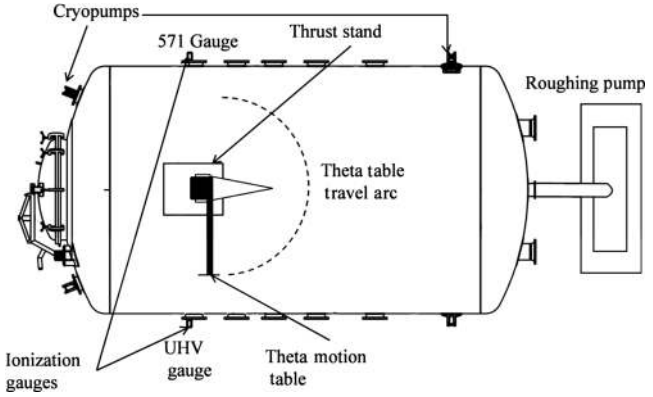

Fig. 5 Vacuum Test Facility 2 at HPEPL.

IV. Experimental Setup

A. Vacuum Facility

All experiments are performed in the Vacuum Test Facility 2 (VTF-2) at the Georgia Institute of Technology High-Power Electric Propulsion Laboratory (HPEPL), which is shown in Fig. 5. VTF-2 is 9.2 m long and 4.9 m in diameter. It is pumped to rough vacuum with one 3800 cubic feet per minute (CFM) blower and one 495 CFM rotary-vane pump. Ten liquid nitrogen cooled CVI TM-1200i reentrant cryopumps with a combined pumping speed of 350,000 l/s on xenon bring the chamber to a base pressure of 1.9×10^{-9} torr. A Stirling Cryogenics SPC-8 RL special closed-looped nitrogen liquefaction system supplies liquid nitrogen to the cryopump shrouds. Two ionization gauges, Varian 571 and UHV-24, are mounted on either side of the chamber. Typical accuracy for ionization gauges is approximately ±20% according to Varian [17].

High-purity (99.9995% pure) xenon propellant is supplied to the HET from compressed gas bottles through stainless steel feedlines. MKS 1179JA mass flow controllers meter the anode and cathode propellant flow. The mass flow controllers have an accuracy of ±1% full scale. The flow controllers are calibrated before each experiment with a custom fixed-volume apparatus that measures gas pressure and temperature as a function of time taking into account the effects of xenon compressibility. Pressure measurements are corrected for xenon using the known base pressure of air and a correction factor of 2.87 for xenon according to the following equation [18]:

$$P_c = \left[\frac{P_i - P_b}{2.87}\right] + P_b \tag{6}$$

where P_c is the corrected pressure on xenon, P_b is the base pressure, and P_i is the indicated pressure when xenon is flowing into the vacuum chamber.

B. Thrust Stand

Thrust is measured with a null-type inverted pendulum thrust stand on the inverted pendulum design developed by the NASA Glenn Research Center [19]. The null-type stand holds the thruster at constant position with use of proportional integral derivative-controlled solenoid coils that move a center magnetic rod. Thrust is correlated to the amount of current on the null coil required to hold the thrust stand at zero. Thrust stand calibration is performed by loading a set of known weights. The resultant linear curve of null-coil current versus weight is used as the conversion for thrust measurements. A copper shroud surrounds the stand. Coolant flow through the shroud and thrust stand structure is used to keep the thrust stand and shroud at a constant temperature. Further details of the thrust stand and its operation can be found in [20]. Between each thrust measurement, the thruster is turned off to record a zero thrust point. Thrust stand calibrations are conducted before and after each series of test data to maximize measurement accuracy. In addition, calibrations are also done if the zero point varied by more than 3 mN between measurements. The uncertainty in the thrust measurement is ±1.4 mN.

C. Hall Thruster

All experiments are performed on the Pratt and Whitney Rocketdyne T-140 laboratory-model HET. The T-140 has an outer diameter of 143 mm, with a nominal thrust of 200 mN at a nominal power rating of 3.4 kW [10]. The discharge channel of the T-140 is made of M26 grade boron nitride. The thruster performance matches the original T-140 thruster at multiple points within 3% of published results. In this work, the thruster was tested in two configurations: in the gas distributor configuration, the discharge power supply is connected to the gas distributor, and in the anode band configuration the discharge power supply is connected to the anode band. With the use of the anode band, the gas distributor electrical connection is removed from the power supply and the anode band is connected. Figure 6 shows a simplified HET electrical schematic for both configurations. Electrical connections enter the chamber through separate feedthrough ports. The thruster discharge power supply is protected by an resistor-capacitor filter consisting of a 1.3Ω resistor in series and a 95 μF capacitor in parallel. The filter acts as a low-pass filter preventing oscillations in the current over 1.4 kHz from reaching the discharge supply.

A LaB_6 cathode, similar in design to ones used in previous HET testing [21], is located at the 12 o'clock position. The cathode orifice is located approximately 70 mm downstream from the outer front pole piece. The cathode flow is fixed at 10% of the anode flow. For all of the experiments, the thruster was operated for 2–3 h after initial exposure to vacuum conditions to allow for outgassing of the discharge chamber walls. If not exposed to the atmosphere, it is operated for 1–2 h at the beginning of the day to allow for thermal equilibrium of the thruster and thrust stand, albeit at different temperatures, before measurements are taken.

Type-K thermocouples are placed on the rear of the gas distributor to measure the anode temperature variation during testing. Thermocouple measurement uncertainty is ±1.1 °C. Two thermocouples are attached to the gas distributor using a combination of ceramic paste (Aremco Products Ceramabond 571) and fiber glass tape. The thermocouples are then covered in a fiber glass sleeve as they exit the thruster. Each thermocouple is electrically isolated with an Omega DRF-TCK voltage-isolating signal conditioner positioned outside

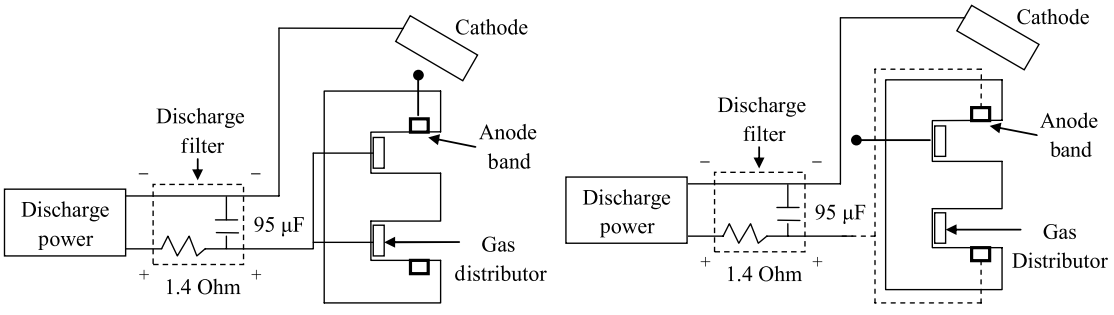

a) Discharge current to gas distributor **b) Discharge current to anode band**

Fig. 6 Electrical schematic of T-140 HET with and without the anode band.

VTF-2. The signal conditioners are calibrated using a thermocouple simulator.

D. Faraday Probe

A Faraday probe is used to measure the ion current density profile of the thruster plume. Figure 7 shows an electrical schematic of the Faraday probe used in this work, which is based on a Jet Propulsion Laboratory design [22]. The probe consists of a tungsten-coated stainless steel collection electrode with a stainless steel guard ring surrounding it. The collector disk is 2.31 cm in diameter. The guard ring and collector are biased −30 V below facility ground to repel electrons. Biasing the guard ring and collector to the same potential minimizes edge effects around the collector by creating a flat uniform sheath such that the effective collection area is equivalent to the geometric area of the collection electrode. Measurements show that this voltage is sufficient for the collector to enter ion saturation without substantial sheath growth [22]. A 1.417 kΩ (±0.5%) resistor is placed in series with the collector line, and the voltage across the resistor is read by an Agilent 24980A data acquisition unit. The probe current is measured to an accuracy of ±0.004% with the resistor. The ion current density is calculated by dividing the current by the collector surface area and has an accuracy of ±0.5%. The distance from the thruster exit plane to the face of the probe is 1.000 ± 0.005 m, with the axis of rotation located on the thruster centerline. Azimuthal sweeps were performed from −90 to 90 deg in 1 deg increments with respect to the thruster centerline (as illustrated in Fig. 5). The angular rotation has an uncertainty of ±0.5 deg. Measurements were taken at an 80 Hz sample rate for 1 s at each position and averaged at each angular position to produce the recorded current density at that location.

E. Retarding Potential Analyzer

The ion energy distribution function is measured with a retarding potential analyzer (RPA) that measures the voltage, relative to facility ground, needed to repel a fraction of the ion population. From this information, the ion energy distribution can be determined [23,24]. The probe acts as a high-pass filter by allowing only ions with voltages, that is, energy-to-charge ratios, greater than the grid voltage to pass and reach a collection electrode. Figure 8 shows an electrical schematic of the probe. RPA primary ion energy peak V_{mp} is corrected by subtracting the plasma potential measurement obtained from an emissive probe (V_p) to calculate true ion potential V_{true}. A loss voltage is computed as the sum of the cathode-to-ground voltage

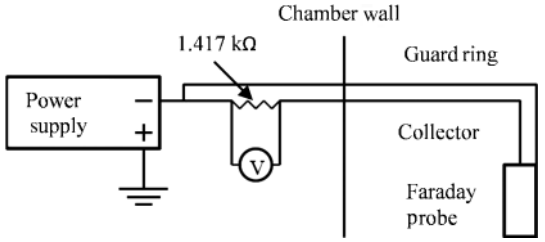

Fig. 7 Faraday probe electrical schematic.

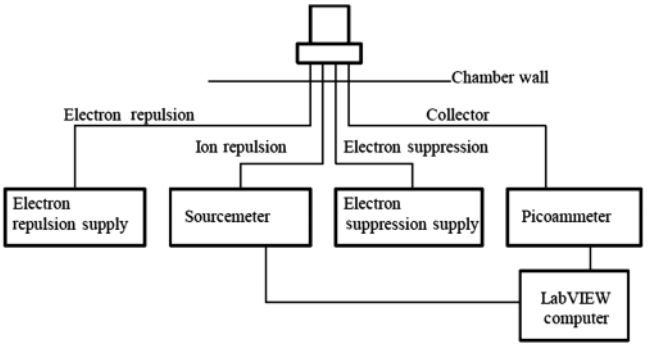

Fig. 8 RPA probe diagram.

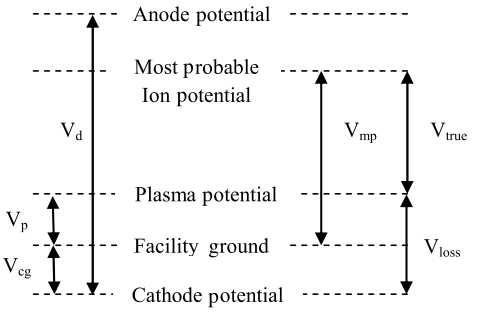

Fig. 9 Potential diagram illustrating the relationship between measured potentials (V_d, V_{cg}), plasma potential measurements (v_{mp}, V_p), and calculated voltages (V_{true}, V_{loss}).

and the plasma potential: $V_{\text{loss}} = |V_{\text{cg}}| + |V_p|$. Figure 9 shows a potential diagram that illustrates the correlation between measured values with the true ion potential. The voltage use efficiency is a measure of the amount of the discharge voltage (potential energy) that is converted into axial ion kinetic energy. This is mathematically defined as the ratio of the acceleration voltage to the discharge voltage, $\eta_v = V_{\text{true}}/V_d$. The data analysis follows the procedure outlined by Hofer and Gallimore [23]. The face of the probe inlet was aligned parallel to the thruster exit plane within an accuracy of ±0.5 deg. The distance from the thruster exit plane to the probe inlet is 1.000 ± 0.005 m. At each ion repulsion grid potential setting, three measurements are taken and averaged. A fourth-order Savitzky–Golay smoothing filter is applied to the raw data before taking the derivative.

F. Floating Emissive Probe

The potentials used to measure the ion energy distribution function obtained from the RPA probe are measured with respect to ground, but the ion energies are determined with respect to the plasma potential. Emissive probes are used to measure the plasma potential to correct the RPA measurements. The probe consists of an exposed electron emissive filament loop, the ends of which are enclosed in a ceramic insulator. A power supply provides current and heats the filament to the point of thermionic emission of electrons. When exposed to the plasma, any probe naturally floats from ground to the floating potential. At the floating potential, a sheath forms around the probe and there is no net current to the probe. This is due to the negative plasma electron current balanced by the positive plasma ion current and secondary electron emission. However, because the emissive probe emits its own electrons, the probe becomes more positive, which in turn draws in more plasma electrons. This process continues until the probe potential reaches the plasma potential. The emitted electron flux that escapes into the plasma decreases as the probe potential increases due to a reduction in the potential hill between the probe and plasma, until the probe reaches the plasma potential or slightly above, at which point emitted electrons return to the probe. The measured probe current plateaus at this point and the probe floats at the plasma potential.

Plasma potential V_p measurements taken with the emissive probe were used to correct the RPA data so that the true ion energy distribution can be computed, i.e., $V_{\text{true}} = V_{\text{RPA}} - V_p$. This corrects for artificially high ion energies due to the aforementioned ground/plasma potential referencing. The emissive probe used in this work consists of a 0.127-mm-diam thoriated-tungsten filament housed in a double-bored alumina tube based on ones used by Haas [21]. The filament loop has a radius of 1.5 mm. Figure 10 shows a schematic of the probe. The voltage difference between the probe and ground is taken at the same time as the RPA measurements. The potential measurements contain an estimated uncertainty of 8%. The distance from the thruster exit plane to the filament is 1.000 ± 0.005 m. It is positioned 3 deg off the thruster centerline with an uncertainty of ±0.5 deg. The floating emissive probe circuit consists of the emissive probe, an isolation amplifier, and a floating power supply capable of supplying enough current (2–3 A) to heat the filament.

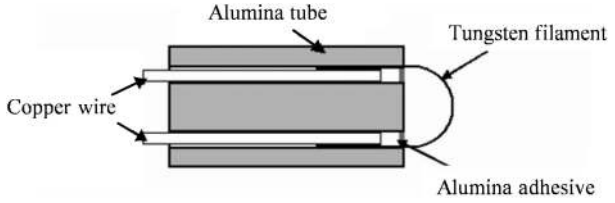

Fig. 10 Schematic of the emissive probe.

V. Experimental Results

Several experiments are conducted to explore the physics of propellant residence time and the effects of anode temperature in the T-140 HET. Figure 11 shows a photograph of the modified T-140 HET with the anode band. Thermal, thrust, and plume measurements of the thruster are conducted at a xenon mass flow rate of 5 mg/s at discharge voltages of 100, 125, and 150 V. The magnetic field is optimized for minimum discharge current for each operating point taken with and without the use of the anode band. No visual change in the thruster plume was noticed due to the separation of the gas distributor and the anode. An additional operating point at 250 V, 8.41 mg/s was tested to allow comparison with published data showing performance matching within 3%. [10]. All differences between the performance of the new T-140 HET and the original thruster, which are with 1% in thrust, 3% in efficiency, and 2% in the T/P ratio, are attributed to manufacturing tolerance and facility effects such as backpressure, choice of cathode, and instrument uncertainties.

A. Thermal Characteristics

Experimental verification of the predicted temperature reduction in the gas distributor was obtained with the use of the anode band. Figure 12 shows the comparison between the rear side gas distributor temperatures with and without the use of the anode band mass flow rate of 5 mg/s. The higher temperatures at 100 and 125 V with and without the use of the anode band, relative to the value at 150 V, are likely due to thruster discharge current instabilities at these low voltages. The thruster plume visually shows occasional flickering, indicating instability in the thruster at these conditions, despite optimization of the magnetic field. The rear side gas distributor temperature measurements agree with the predictions of the thermal model at the same physical location. The difference between the rear side gas distributor temperature with and without the use of the anode band corresponds to a 270 K drop in temperature on the front face of the gas distributor.

B. Thruster Performance

Thruster performance measurements are taken to investigate propellant residence time impact on thrust, efficiency, and discharge current. With the mass flow rate set to 5 mg/s, the voltage was varied from 100 to 150 V. The thruster was first tested with the discharge current collected by the gas distributor. The gas distributor collects the full current, whereas the anode band is completely disconnected

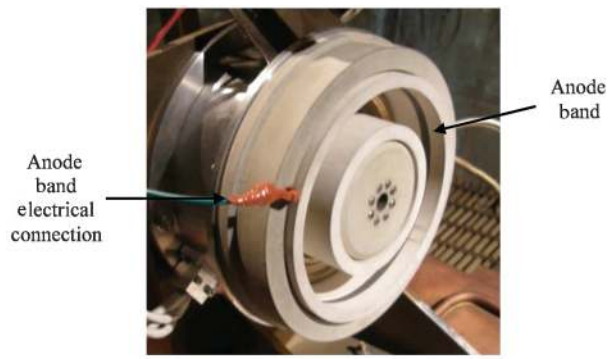

Fig. 11 T-140 HET with the anode band embedded into the discharge chamber.

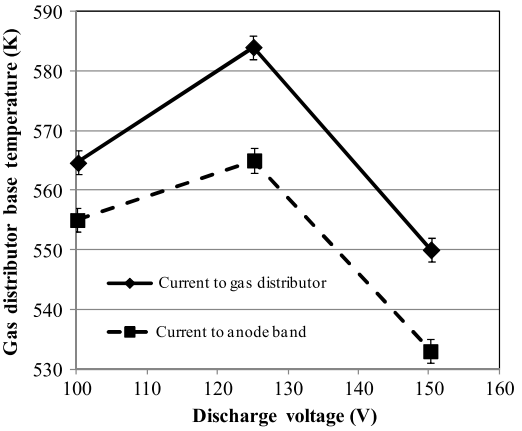

Fig. 12 Measured gas distributor rear temperatures at 5 mg/s as functions of discharge voltage for discharge current to gas distributor and anode band.

from the power supply, i.e., electrically floating. In this way, the anode band floats at the local plasma potential. Raitses et al. showed the plasma potential shifts upstream with the presence of floating graphite electrodes [16]. In addition, the placement of the anode band upstream of the magnetic field ensures that it is not exposed to high electron temperature. This makes the difference in secondary electron emission between the inconel and boron nitride channel less important. The magnetic field is optimized for each data point for minimum discharge current.

When the discharge current is collected by the embedded anode band (the anode band configuration), the gas distributor electrical connection is removed, i.e., the gas distributor is floating, and it is connected to the anode band (as shown in Fig. 6b). Therefore, the gas distributor is allowed to float to the local floating potential of the plasma and has an insignificant effect on the potential inside the thruster channel. At the floating potential, a sheath forms over the gas distributor and there is no net current to the gas distributor. Data were collected at 5.1 mg/s at 100, 125, and 150 V, and the magnetic field is reoptimized at each point. The magnet currents for the two configurations are different. The magnetic field from the gas distributor configuration results in a decrease in thrust and efficiency when used with the anode band configuration and results in unstable operation. The primary change in the magnetic field is a 3–4 A reduction in the outer coil current and a 1–3 A reduction in the inner coil current. After the initial set of low-voltage data were collected, it became difficult to maintain the current on the anode band without the current level spiking up. The likely reason is that the secondary electron emission from the inconel band material increases as the band temperature rises. This prevented high-voltage operation beyond ~10 min with the anode band configuration. However, the data are repeatable over the course of several days of testing. After the initial thruster conditioning sequence is completed and the thruster has completely outgassed, the performance of the thruster (such as the discharge current at a given flow rate) is always repeatable, and steady state is reached within 1 min of reaching the optimized magnetic field setting.

Figure 13 shows the thrust and T/P ratio as a function of discharge voltage for the two configurations with the current collected by the gas distributor and the current collected on the embedded anode band. To take into account the reduced magnetic field strength of the anode band configuration, the T/P ratio is defined as the thrust divided by the sum of the discharge power (discharge current times discharge voltage). Within the experimental uncertainty, no changes in the thrust and T/P ratio are observed by the use of the anode band. Changes in the thrust data before and after the gas distributor temperature reduction agree with the previous study using an actively cooled anode [5]. Figure 14 illustrates the increase in discharge current I_d recorded with the use of the anode band at constant mass flow rate $\dot{m}_a$.

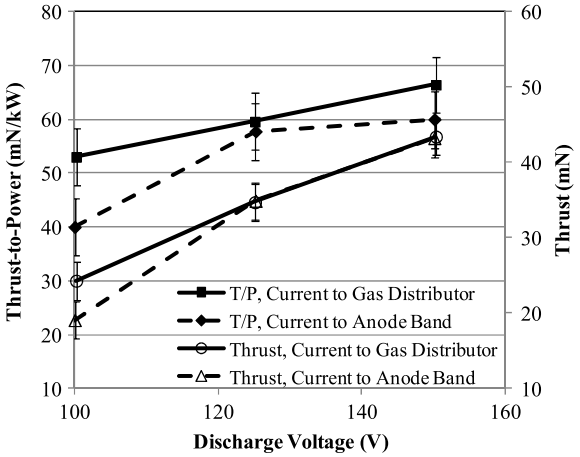

Fig. 13 Thrust and T/P ratio as a function of discharge voltage at 5 mg/s. Both the configurations (current collected on gas distributor and current collected on anode band) are shown.

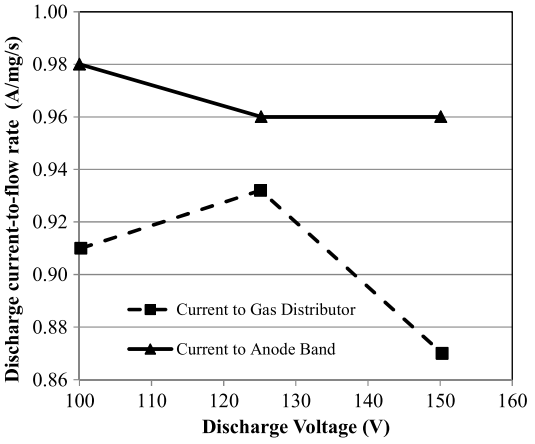

Fig. 14 $I_d/\dot{m}_a$ as a function of discharge voltage at 5 mg/s with the current collected on the gas distributor vs the anode band.

C. Plume Properties

At each voltage, the thruster plume was characterized with the RPA, emissive probe, and the Faraday probe. Table 2 shows the results of the plume diagnostics. A 10% increase in the peak current density is measured by the Faraday probe when the current is collected by the anode band. This increase in the ion current density is an indication of an increase in propellant use, which is likely a direct consequence of increased propellant residence time. The increase in discharge current for the anode band configuration also supports this conclusion. Figure 15 shows ion current density profiles at 150 V, 5 mg/s both with and without the use of the anode band. Faraday probes typically overestimate the ion current density at large angles from the thruster centerline due to the presence of low-energy charge exchange (CEX) ions. Shifting the current to the anode band showed

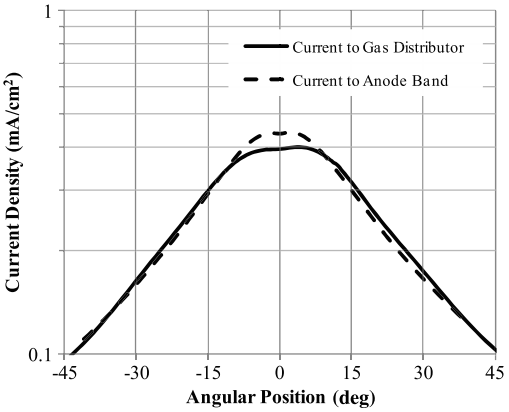

Fig. 15 Comparison of ion current density profiles at 150 V, 5 mg/s for current collected on the anode band and gas distributor.

no change in the CEX current contribution at high angles, as revealed by the lack of current density change at angles beyond 30 deg; therefore, the increase in the centerline ion current density also corresponds to an increase in the ion beam current. Measurements of the plasma potential and ion loss voltage are slightly lower for the anode band configuration compared with the gas distributor configuration. Figure 16 shows the plasma potential with respect to facility ground versus the discharge voltage.

Ion energy and plasma potential measurements were taken at each test point along that thruster centerline. Figure 17a shows the ion energy distribution function on the thruster centerline at 150 V, 5 mg/s. The profiles show that the ion energy distribution function broadens when the current is collected on the anode band and the peak significantly decreases. One possible source of a broader ion energy distribution function is an increase in the length of the ionization zone, which results in a larger spread in ion energies, leading to increased plume divergence. However, this has only been observed in configurations in which the current is collected at the rear of the discharge channel. The anode band data in Fig. 17a is not collected in that configuration. Detailed plume divergence data are required to understand the cause of the increase in the width of the ion energy distribution. There is a reduction in the primary ion energy peak of 4.5 V with the use of the anode band. The uncertainty due to the smoothing algorithm in the RPA analysis is estimated to be $\pm 1\%$. The uncertainty in the most probable ion potential is estimated as 50% of the half-width at half-maximum value of the potential peak [25]. This uncertainty varies depending on discharge voltage and has a maximum value of ± 6.5 V.

Figures 17b and 17c show the ion energy distributions at 100 and 125 V and 5 mg/s. For the 125 V case, the probable voltage increases by approximately 5.75 V when current is collected by the anode band. This increase in the primary ion energy peak is in agreement with the increase in the T/P ratio obtained at this condition, as shown in Fig. 13. At 100 V, a reduction of 6.5 V in the most probable voltage is measured with the use of the anode band compared with when the current is collected by the gas distributor. The 100 V, 5 mg/s operating condition was the final data point collected during the test series due to difficulty in maintaining the current on the anode band.

Table 2 T-140 HET operating conditions and plume properties with and without the use of the anode band

V_d, V	I_d, A	Gas distributor temperature, K	V_p, V	V_{loss}, V	v_{mp}, V	η_v	FWHM, V	Peak current density, mA/cm²
Current collected on gas distributor with anode band floating								
100.2	4.55	565	11.4	31	61.5	0.66	12.0	0.21
125.1	4.66	584	12.9	33	81.1	0.71	16.0	0.28
150.3	4.35	550	14.3	36	104.7	0.74	17.0	0.40
Current collected on anode band								
100.1	4.90	555	10.7	30	55.0	0.65	15.0	— —
125.2	4.80	565	12.1	31	86.9	0.74	20.0	0.30
150.2	4.80	533	12.7	33	100.2	0.75	32.0	0.45

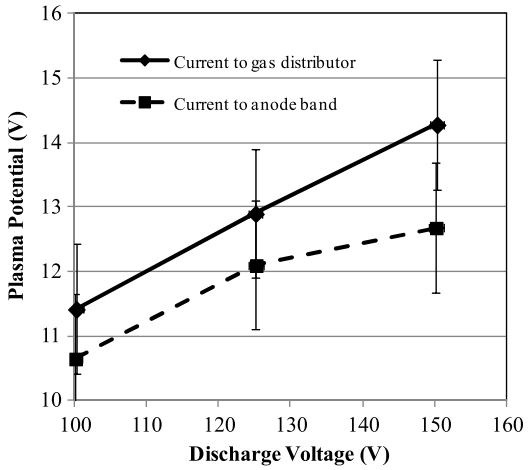

Fig. 16 Plasma potential as a function of discharge voltage at 5 mg/s anode flow rate, 1 m downstream of the thruster exit plane for discharge current on gas distribution and anode band.

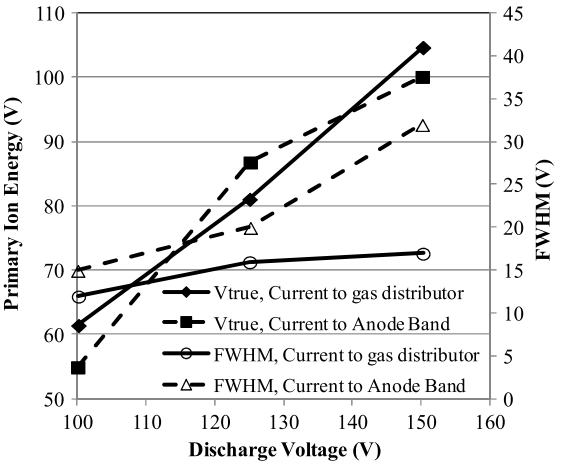

Fig. 18 Primary ion energy and FWHM measurements at 5 mg/s for 100, 125, and 150 V.

Therefore, the 100 V test point is the only one for which the magnetic field is not completely optimized. All other test points are fully optimized.

Figure 18 shows the primary ion energy peak and the full-width at half-maximum (FWHM) value for discharge voltages of 100, 125, and 150 V with and without the use of the anode band. The general trends are as expected with both the primary energy peak and the FWHM increasing with voltage.

VI. Discussion

A. Collision Frequency and Electron Mobility

For efficient ionization, the neutral residence time should be much longer than the time between electron–neutral impact ionization collisions. For collisional plasmas, the cross-field electron diffusion coefficient is proportional to the frequency of collisions between electrons and other species in the plasma [26]. Therefore, the electron–neutral, electron–ion, and electron–wall collision frequencies each affect the electron mobility in a HET, which is driven by the electron diffusion coefficient. The temperature of the injected neutrals has a negligible impact on the electron–ion collision frequency, because once a neutral is ionized its behavior is determined largely by its interaction with the local electric field. The flux of the neutral particles in the axial direction is obtained from [27] as

$$\Gamma = \frac{1}{4} n_n V_n = \frac{1}{4} n_n \sqrt{\frac{8 k_B T_n}{\pi m_{xe}}} \tag{7}$$

where n_n is the neutral density, V_n is the neutral velocity, and T_n is the temperature of the neutral particles.

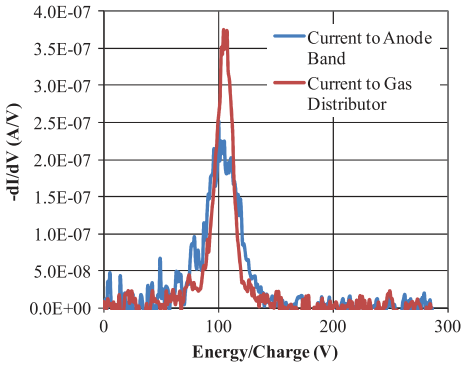

a) 150 V, 5 mg/s

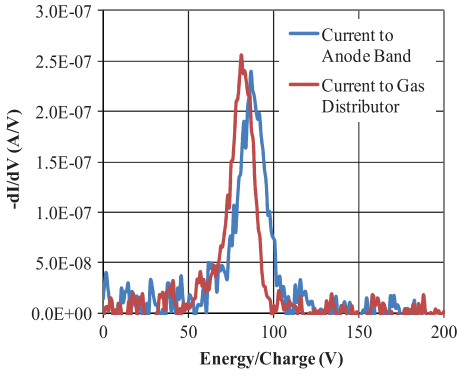

b) 125 V, 5 mg/s

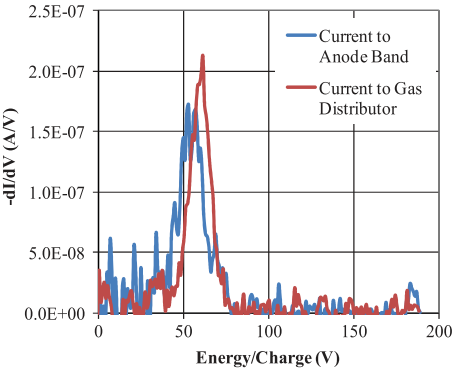

c) 100 V, 5 mg/s

Fig. 17 Ion energy distributions at 5 mg/s for 100, 125, and 150 V.

One result from mass conservation is that if the flow rate is kept constant (such as it is here at 5 mg/s) the axial flux of neutrals is also constant. Equation (7) thus means that the neutral density is inversely proportional to the square root of the temperature. The electron–neutral collision frequency is expressed by

$$\nu_{\text{en}} = n_n \sigma_{\text{en}} V_e = n_n \sigma_{\text{en}} \sqrt{\frac{8k_B T_e}{\pi m}} \tag{8}$$

where T_e is the electron temperature. We see from Eq. (8) that an increase in the neutral density will increase the neutral–electron collision frequency, because the collision cross section and the electron velocity are essentially independent of the neutral propellant temperature. The neutral density will decrease in the ionization zone, but Eq. (8) is taken to be an overall average over the entire channel length.

Based on the projected reduction of the gas distributor face temperature when discharge heating is removed, an increase in the electron–neutral collision frequency of approximately 25% is achieved. The increase in the electron–neutral collision frequency is expected to improve the propellant use, which leads to an increase in the ion current density, as shown in Table 1. However, the data point to possibly multiple effects from the separation of the current collection site and the gas distributor. An increase in the discharge current with the use of the anode band can be caused by a number of factors, including increased propellant use, increased electron mobility, and an increase in the percentage of doubly charged ions.

The measured increase in beam current and discharge current with the anode band indicates that the thruster uses a larger percentage of the propellant relative to the gas distributor configuration. However, the fact that the thrust did not increase at a constant mass flow rate rules out an increase in propellant use as the only explanation.

Another possibility is a change in electron mobility. Cross-field electron mobility can be viewed as a measure of how many electrons are able to escape the magnetic field in the thruster and strike the anode. It is a major source of efficiency loss at low voltages, as each electron that strikes the anode must be reemitted by the thruster cathode, thus costing power. Given that the physical placement of the anode band is much closer to the Hall current maximum, the electrons have a shorter path to the anode band then to the gas distributor. Therefore, one can expect higher electron mobility effects with the use of the anode band configuration. As stated earlier, the placement of the anode band is based on a balance between maximizing the temperature reduction of the gas distributor and encroaching on the Hall current region. Electron mobility increases manifest as an increase in discharge current with no increase in thrust or beam current. The thrust did not change, and discharge current increased by 6–10% with the anode band, but there is a sizable increase in the beam current as well. Therefore, the electron mobility alone cannot account for the increased discharge current, as the beam current also increased.

Finally, an increase in the level of multiply charged ions is considered, because conditions that tend to increase propellant use, such as ionizing collision frequencies, also increase the likelihood of multiply charged ions. This would result in an increase in thrust, discharge current, and beam current. Because each multiple ion would produce multiple electrons, one expects that the beam and discharge currents would increase at exactly the same rate. Although the discharge current and beam current increase, they are at different rates and the thrust did not increase. The electron temperature is approximately 10% of the discharge voltage, which typically benefits the ionization efficiency for operation above 300 V because the ionization cross section of xenon by electron impact maximizes with electron energy in the range 40–90 eV [13]. The ionization potential is 12 eV from Xe to Xe^+ and 21 eV from Xe^+ to Xe^{2+}. At the low voltages tested for this study, 100–150 V, an insignificant amount of doubly charged ions is created by the high-energy tail of these Maxwellian electrons. The absence of a peak in the RPA scan at energies above the primary energy peak also provides no evidence of effects from multiply charged ions.

Although the increased electron–neutral collision frequency improves propellant use, causing an increase in the beam current, the greater effect could be enhanced electron mobility and an increase in the electron flux to the anode, leading to the elevated discharge current at flow rate ratios seen in Fig. 14. It seems likely that a reduction in the electron mobility could be achieved if the anode band is placed further upstream. This would allow the improved propellant use to translate as an increase in thruster efficiency. The broader ion energy distribution seen in Fig. 17a could indicate that the use of the anode band increases the ionization zone length, which results in a larger spread in ion energies, i.e., larger beam FWHM. A longer ionization zone can increase the spread of slow ions, which increase the plume divergence. However, due to the lack of a complete set of Faraday probe scans for these operating conditions, no conclusive statements can be made about the cause for the increase in the width of the ion energy distribution function.

Enhanced electron mobility causes the electrons to better ionize the gas over a greater volume of the discharge channel, leading to an increase in the ionization zone length. If electrons are able to cause ions to be born further downstream in the acceleration zone and in the fringe electric fields, then these ions would produce little or no thrust compared with ones only born in the region of the full plasma potential along the centerline of the channel upstream of the acceleration zone. This would cause the larger beam current without a thrust increase.

B. Neutral Velocity and Wall Effects

To determine the impact of the wall temperature on the neutral velocity, the flow regime of the neutral gas can be determined by the Knudsen number (Kn), given by

$$Kn = \frac{\lambda}{L} \tag{9}$$

where λ is the mean free path of the particles and L is the characteristic length scale. For neutral flow in a Hall thruster, L is typically the width or the length of the discharge channel. A continuum flow is represented by a Knudsen number of less than 0.1, whereas free molecular flow is represented by a Knudsen number of greater than 10. The transitional regime is taken to be at a Knudsen number between 0.1 and 10.

To calculate the Knudsen number, we let L be the length of the channel and calculate the mean free path via Eq. (10):

$$\lambda = \frac{1}{\sqrt{2} n_n \sigma} \tag{10}$$

where n_n is the neutral density, σ is the collisional cross section, and $\sqrt{2}$ accounts for collisions between two particles of the same Maxwellian-like distribution. The neutral density can be calculated by using Eq. (11):

$$n_n = (1 - f_i) \frac{(\dot{m}_a/m)}{A_C V_n} \tag{11}$$

where f_i is the fraction of xenon from the anode that has been ionized at the given location, $\dot{m}_a$ is the anode mass flow rate, m is the mass of xenon, and A_C is the channel cross-sectional area. To simplify the calculation, we use only Eq. (11) in the regime upstream of where the ionization zone resides and assume $f_i = 0$.

The Knudsen number ranges from 0.55 without the anode band and 0.34 with the anode band in the area immediately in front of the gas distributor, which means the flow regime there is transitional. Because density measurements taken inside a Hall thruster show that the neutral density is reduced by about two orders of magnitude due to ionization in the downstream half of the channel, we can deduce that the flow regime becomes free molecular near the exit plane [28].

In the free-molecular limit, the neutrals only collide with the chamber wall. Because neutral xenon has a very high accommodation factor when striking the boron nitride wall [29], they will leave

at approximately the same energy as the location of impact on the wall. Let the aspect ratio of the discharge channel be defined as the channel length divided by channel width. The fraction of the neutral xenon that undergoes no collisions before exiting the thruster is 16% for a channel aspect ratio of 2 (corresponding to the T-140 HET). This number can be calculated by assuming the particles radiate out from the gas distributor in a semicircular manner. All other particles will interact with the wall before exiting the discharge channel. Assuming the extreme case in which these interacting particles all thermalize with the wall, they will all exit the channel with roughly the same temperature and bulk velocity, whereas the particles that do not interact will exit at anode temperature and their initial velocities.

Discharge chamber temperature data at thruster conditions similar to the ones tested for this study have shown peak wall temperatures in excess of 770 K [30]. Given that the use of the anode band results in a gas distributor exit plane temperature of less than 575 K for all the operating points tested, heating of the neutral propellant from impact with the wall will increase the neutral velocity by as much as 25% compared with the velocity at the gas distributor exit plane. Because the wall temperature increases downstream of the gas distributor, the neutral velocity will correspondingly increase as well. Given that the flow is transitional in the upstream half of the channel, the wall temperature likely plays a nonnegligible role in accelerating the neutral particles, as measured by several researchers [30–32].

The initial reduction in the neutral velocity through the use of the anode band is partially counteracted by the high temperature of the walls, which cause the neutrals to accelerate downstream of the gas distributor. The nearly identical thrust between the anode and gas distributor configurations agrees with recent data of a modified HET with a similar current collecting anode band [33]. An active cooling system to reduce the temperature of the discharge channel walls may be necessary to fully capitalize on the reduction in neutral velocity at the gas distributor from the use of the anode band. In addition, placement of the magnetic field peak, which has been predicted to correlate with maximum wall temperature, slightly downstream of the channel exit plane could allow for reduced peak wall temperatures and sustain a larger propellant residence time throughout the discharge chamber [34]. For reference, the T-140 HET has the magnetic field peak at the channel exit plane.

Were it not for the wall effects, the total thruster efficiency would be estimated to increase by approximately 5.5%. However, with the majority of the neutrals colliding with the wall before exiting the thruster, an efficiency improvement of no more than 2.5% is expected due to acceleration of the neutrals upon leaving the gas distributor. The enhanced electron mobility likely eliminates this improvement, resulting in the negligible change in efficiency and the thrust-to-power ratio when collecting the discharge current on the anode band instead of the gas distributor.

C. Ionization Zone Length

The impact of the ionization zone length on propellant use is studied specifically through the use of the RPA probe. Reference [35] reports that elevated neutral temperature will lengthen the ionization zone and decrease the amplitude of the breathing mode oscillation. The expected opposite scenario is that that a reduction in the neutral temperature would decrease the ionization zone and possibly increase the amplitude of the breathing mode oscillations. During testing of the T-140 HET, increased levels of discharge current oscillations are noticed through visual observations of the power supply discharge current readout when using the anode band. Measurements of the discharge current oscillations are not recorded. However, a reduction in the neutral temperature does not lead to the expected contraction of the ionization zone based on RPA measurements.

The dispersion efficiency characterizes the effect of the spread in ion velocities in the Hall thruster plume and is expressed as [36]

$$\eta_d = \frac{\langle V_i \rangle^2}{\langle V_i^2 \rangle} \tag{12}$$

where $\langle V_i \rangle$ is the average ion velocity. Examples of the spread in ion energy per charge on the thruster centerline are shown in Fig. 17. The dispersion efficiency can be characterized by the FWHM of the ion voltage distribution, allowing for the observation of the relative variation of this efficiency term. In other words, the energy loss is mainly a combination of spread in the energy-per-charge distribution function (the dispersion efficiency) and can be evaluated quantifiably by studying the trends in the FWHM of the ion voltage distribution. As shown in Fig. 18, use of the anode band results in a rapid rise in the FWHM above 125 V, whereas it tends to stay nearly constant when current is collected on the gas distributor. This behavior more than counteracts the impact of any reduction of the voltage loss term due to the use of the anode band. The 100 V case is never fully stable. Numerical modeling shows that as the voltage is reduced the ionization region expands, which causes a reduction in the propellant use [37,38]. The 150 V case is significantly more affected by the rise in the FWHM than the lower voltages. A larger FWHM of the ion voltage distribution leads to a wider ionization region, which reduces propellant use [39,40]. A wider ionization zone increases the spread of ion energies, including slow ions, which can enlarge the plume divergence and reduce thruster efficiency and lifetime due to increased wall losses. This could help explain the decrease in the anode efficiency seen in the actively cooled anode configuration tests performed above 150 V in [5]. Incorporating a magnetic field profile with a steeper axial gradient of the radial magnetic field than the one used for the T-140 HET could counteract these wall losses [13].

Another indication of the change in the ionization zone and possibly the acceleration zone is the reduction in the plasma potential shown in Fig. 16 for the anode band configuration. Hofer and Gallimore report a similar drop in the plasma potential corresponding to a decrease in the magnetic field of 5–10% of the peak at the exit plane, which matches the level of reduction seen when shifting the current to the anode band [23]. However, the change in the plasma potential and optimum magnetic field for the anode band could be a result of a shift in the ionization and acceleration zones due to the physical location of the anode band. The acceleration region is the axial length where the majority of the potential drop occurs and ions are accelerated by the electric field. Raitses *et. al.* reports that the plasma potential shifts upstream with the presence of a graphite anode band, indicating a shift of the ionization and acceleration region as well [41]. This change is attributed to a lower secondary electron emission compared with the BN channel, which alters the electron temperature. The presence of a conductive layer on the opposite wall from the anode band location is confirmed with an ohm meter. In other words, the band material was sputtered onto the opposite wall, increasing the extent of the channel surface with a lower secondary electron emission coefficient. The inconel material used for the anode band also has a lower secondary electron emission compared with the BN, but the extent of the shift in the ionization and acceleration zones requires further investigation to better quantify the interactions. It was thought that the placement of the single anode band on the outer wall outside the bulk Hall current region and upstream of the maximum magnetic field strength would eliminate any perturbations of the plasma. However, the changes in the required optimum magnetic field strength represent a small disturbance caused by the anode band location, which reduces the plasma potential.

VII. Conclusions

The primary heating mechanism for the Hall-effect thruster gas distributor is removed by collecting the discharge current on a separate anode band placed downstream of the gas distributor. The physics governing the relationship between anode temperature and ionization fraction seems to be a combination of competing effects involving propellant use, electron mobility, and wall thermalization. Each thruster operating condition reveals a 10% increase in peak ion current density when using the anode band to collect the current instead of the gas distributor. The reduction in neutral velocity yields an increase in neutral number density, which increases the electron–neutral collision frequency. However, one result is enhanced electron mobility, which leads to an increased electron flux to the anode band

consistent with the elevated discharge current to flow rate ratio. The larger discharge current is due to the placement of the anode band being physically much closer to the maximum Hall current region, which provides a shorter path to the positive electrode for the electrons in comparison with the anode/gas distributor configuration. Perhaps a different anode band position relative to the Hall current could alleviate this issue by reducing the electron mobility and preventing ions from being born downstream of the acceleration zone or in the fringe electric fields. This may lead to the higher T/P ratio one would expect from the measured increase in beam current.

Retarding potential analyzer measurements suggest that the ionization zone may start closer to the gas distributor when the discharge current is collected on the anode band for voltages above 125 V, which leads to larger wall losses. However, at voltages below 125 V, the experimental data suggest that the predicted efficiency increase due to the reduction in the neutral velocity is partially counteracted by wall thermalization that occurs as the neutrals move further downstream. With the reduction in gas distributor temperature and therefore the injection of lower velocity neutrals relative to those exiting the gas distributor without the use of the anode band, the chamber wall could play a dominant role in neutral flow dynamics by heating up the bulk of the neutral population. Thus, increasing propellant residence time for the length of the channel upstream of the acceleration zone may require a reduction in the temperature of both the gas distributor and the walls.

Acknowledgments

Support for this research is provided by American Pacific Corporation In-Space Propulsion. The authors would like to thank Pratt and Whitney Rocketdyne for supplying the Georgia Institute of Technology High-Power Electric Propulsion Laboratory (HPEPL) with the T-140, Hoang Dao for assistance during thruster installation and testing, and departmental technical staff and other graduate students at HPEPL for assistance with this work.

References

[1] Byers, D. C., and Dankanich, J. W., "Geosynchronous-Earth-Orbit Communication Satellite Deliveries with Integrated Electric Propulsion," *Journal of Propulsion and Power*, Vol. 24, No. 6, 2008, pp. 1369–1375. doi:10.2514/1.35322

[2] Linnell, J. A., and Gallimore, A. D., "Efficiency Analysis of a Hall Thruster Operating with Krypton and Xenon," *Journal of Propulsion and Power*, Vol. 22, No. 6, 2006, pp. 1402–1412. doi:10.2514/1.19613

[3] Wilbur, P. J., and Brophy, J. R., "The Effect of Discharge Chamber Wall Temperature on Ion Thruster Performance," *AIAA Journal*, Vol. 24, No. 2, 1986, pp. 278–283. doi:10.2514/3.9257

[4] Kieckhafer, A. W., Massey, D. R., and King, L. B., "Performance and Active Thermal Control of 2-kW Hall Thruster with Segmented Electrodes," *Journal of Propulsion and Power*, Vol. 23, No. 4, 2007, pp. 821–827. doi:10.2514/1.21820

[5] Book, C., and Walker, M. L. R., "Effect of Anode Temperature on Hall Effect Thruster Performance," *Journal of Propulsion and Power*, Vol. 26, No. 5, 2010, pp. 1036–1044. doi:10.2514/1.48028

[6] Reid, B., and Gallimore, A., "Review of Hall Thruster Neutral Flow Dynamics," IEPC Paper 07-038, 2007.

[7] Jacobson, D. T., Manzella, D. H., Hofer, R. R., and Peterson, P. Y., "NASA's 2004 Hall Thruster Program," AIAA Paper 2004-3600, 2004.

[8] Arhipov, B. A., Krochak, L. Z., and Maslennikov, N. A., "Thermal Design of the Electric Propulsion System Components: Numerical Analysis and Testing at Fakel," AIAA Paper 1998-3489, 1998.

[9] Arhipov, B. A., Krochak, L. Z., Kudriacev, S. S., Murashko, V. M., and Randolph, T., "Investigation of the Stationary Plasma Thruster (SPT-100) Characteristics and Thermal Maps at the Raised Discharge Power," AIAA Paper 1998-3791, 1998.

[10] Mclean, C. H., McVey, J. B., and Schappell, D. T., "Testing of a U.S.-Built HET System for Orbit Transfer Applications," AIAA Paper 1999-2574, 1999.

[11] Mazouffre, S., Echegut, P., and Dudeck, M., "A Calibrated Infrared Imaging Study on the Steady State Thermal Behavior of Hall Effect Thrusters," *Plasma Sources Science and Technology*, Vol. 16, No. 1, 2007, pp. 13–22. doi:10.1088/0963-0252/16/1/003

[12] Roche, S., Barral, S., Bechu, S., Dudeck, M., Lasgorceix, P., Magne, L., Minea, T., Pagnon, D., and Touzeau, M., "Thermal Analysis of a Stationary Plasma Thrusters," AIAA Paper 1999-2296, 1999.

[13] Hofer, R. R., "Development and Characterization of High-Efficiency, High-Specific Impulse Xenon Hall Thrusters," Ph.D. Dissertation, Dept. of Aerospace Engineering, Univ. of Michigan, Ann Arbor, MI, Jan. 2004.

[14] COMSOL Multiphysics, Ver. 3.5a, COMSOL, Burlington, MA, Dec. 2008.

[15] Haas, J. M., and Gallimore, A. D., "Considerations on the Role of the Hall Current in a Laboratory-Model Thruster," AIAA Paper 2001-3507, 2001.

[16] Raitses, Y., Keidar, M., Staack, D., and Fisch, N. J., "Effects of Segmented Electrode in Hall Current Plasma Thrusters," *Journal of Applied Physics*, Vol. 92, No. 9, 1 Nov. 2002, pp. 4906–4911. doi:10.1063/1.1510556

[17] "Vacuum Measurement," Product Catalog Varian, Inc. Vacuum Technologies, Palo Alto, CA, 2003, http://www.varianinc.com/cgi-bin/nav?products/vacuum/measure/gauges=JPLHPIHFO.

[18] Dushman, S., and Lafferty, J. M., *Scientific Foundations of Vacuum Technique*, 2nd ed., Wiley, New York, 1962, pp. 301–346.

[19] Haag, T. M., and Osborn, M, "RHETT/EPDM Performance Characterization," IEPC Paper 97-107, 1997.

[20] Xu, K. G., and Walker, M. L. R., "High-Power, Null-Type, Inverted Pendulum Thrust Stand," *Review of Scientific Instruments*, Vol. 80, No. 5, May 2009, pp. 1–6. doi:10.1063/1.3125626

[21] Haas, J. M., "Low-Perturbation Interrogation of the Internal and Near-Field Plasma Structure of a Hall Thruster Using a High-Speed Probe Positioning System," Ph.D. Dissertation, Dept. of Aerospace Engineering, Univ. of Michigan, Ann Arbor, MI, 2001.

[22] Walker, M. L. R., Hofer, R. R., and Gallimore, A. D., "Ion Collection in Hall Thruster Plumes," *Journal of Propulsion and Power*, Vol. 22, No. 1, 2006, pp. 205–209. doi:10.2514/1.11953

[23] Hofer, R. R., and Gallimore, A. D., "High-Specific Impulse Hall Thrusters, Part 2: Efficiency Analysis," *Journal of Propulsion and Power*, Vol. 22, No. 4, July–Aug. 2006, pp. 732–740. doi:10.2514/1.15954

[24] Hutchinson, I. H., *Principles of Plasma Diagnostics*, 1st ed., Cambridge Univ. Press., Cambridge, England, U.K., 1987, pp. 223–227.

[25] Brown, D. L., "Investigation of Low Discharge Voltage Hall Thruster Characteristics and Evaluation of Loss Mechanism," Ph.D. Dissertation, Univ. of Michigan, Ann Arbor, MI, 2009.

[26] Chen, F. F., "Diffusion and Resistivity," *Plasma Physics and Controlled Fusion*, 2nd ed., Springer–Verlag, New York, 2006, Vol. 1, p. 172.

[27] Goebel, D., and Katz, I., "Electric Propulsion: Ion and Hall Thrusters," *Basic Plasma Physics*, Wiley, Hoboken, NJ, 2008, pp. 43–60.

[28] Cedolin, R. J., Hargus, W. A., Storm, P. V., Hanson, R. K., and Cappelli, M. A., "Laser-Induced Fluorescence Study of a Xenon Hall Thruster," *Applied Physics B*, Vol. 65, No. 4, 1997, pp. 459–469. doi:10.1007/s003400050297

[29] Huang, W., Gallimore, A. D., and Hofer, R. R., "Neutral Flow Evolution in a Six-Kilowatt Hall Thruster," *Journal of Propulsion and Power*, Vol. 27, No. 3, 2011, pp. 553–563. doi:10.2514/1.54141

[30] Hargus, W. A., and Cappelli, M. A., "Laser-Induced Fluorescence Measurements of Velocity within a Hall Discharge," *Applied Physics B*, Vol. 72, No. 8, 2001, pp. 961–969. doi:10.1007/s003400100589

[31] Agrawal, A., and Prabhu, S. V., "Survey on Measurement of Tangential Momentum Accommodation Coefficient," *Journal of Vacuum Science and Technology A*, Vol. 26, No. 4, 2008, pp. 634–645. doi:10.1116/1.2943641

[32] Lejeune, A., Dannenmayer, K., Bourgeois, G., Mazouffre, S., Guyot, M., and Denise, S., "Impact of the Channel Width on Hall Thruster Discharge Properties and Performances," IEPC Paper 2011-019, 2011.

[33] Peterson, P. Y., Massey, D. R., Shabshelowitz, A., Shastry, R., and Liang, R., "Performance and Plume Characterization of a Helicon Hall Thruster," IEPC Paper 2011-269, 2011.

[34] Katz, I., Mikellides, I. G., and Hofer, R. R., "Channel Wall Plasma Thermal Loads in Hall Thrusters with Magnetic Shielding," AIAA Paper 2011-608, 2011.

[35] Furukawa, T., Miyasaka, T., and Fujiwara, T., "Methods of Controlling Low-Frequency Oscillation in a Hall Thruster," IEPC Paper 2001-057, 2001.
[36] Kim, V., "Main Physical Features and Processes Determining the Performance of Stationary Plasma Thrusters," *Journal of Propulsion and Power*, Vol. 14, No. 5, 1998, pp. 736–743. doi:10.2514/2.5335
[37] Ahedo, E., and Escobar, D., "Influence of Design and Operation Parameters on Hall Thruster Performances," *Journal of Applied Physics*, Vol. 96, No. 2, 15 July 2004, pp. 983–992. doi:10.1063/1.1759790
[38] Irishkov, S. V., Gorshkov, O. A., and Shagayda, A. A., "Fully Kinetic Modeling of Low-Power Hall Thrusters," IEPC Paper 2005-035, 2005.
[39] Ahedo, E., and Escobar, D., "Influence of Design and Operation Parameters on Hall Thruster Performances," *Journal of Applied Physics*, Vol. 96, No. 2, 15 July 2004, pp. 983–992. doi:10.1063/1.1759790
[40] Irishkov, S. V., Gorshkov, O. A., and Shagayda, A. A., "Fully Kinetic Modeling of Low-Power Hall Thrusters," IEPC Paper 2005-035, 2005.
[41] Raitses, Y., Dorf, L. A., Litvak, A. A., and Fisch, N. J., "Plume Reduction in Segmented Electrode Hall Thruster," *Journal of Applied Physics*, Vol. 88, No. 3, 1 Aug. 2000, pp. 1263–1270. doi:10.1063/1.373813

J. Blandino
Associate Editor